

Validation of a method for determining the depth of glacial melt ponds using satellite imagery

William A. SNEED, Gordon S. HAMILTON

Climate Change Institute, University of Maine, 303 Bryand Global Sciences Center, Orono, ME 04469-5790, USA
E-mail: william.sneedjr@maine.edu

ABSTRACT. In situ measurements of water depth and optical properties of a melt pond in East Greenland were collected to verify a previously developed algorithm for determining supraglacial water depths using satellite imagery. That algorithm made five simplifying assumptions which we have tested using the in situ data and laboratory analysis of water samples. We conclude that three assumptions were justified, one was not and the remaining one (substrate homogeneity) requires further study, but probably has a minor effect on the retrieved water depths and volumes. Measured water depths of 0.2–3.0 m agree well with those derived from a satellite image using the algorithm. Numerically modeled depths also agree well with those from the satellite image. This new analysis demonstrates the validity of our algorithm as a means for determining meltwater volumes in supraglacial ponds and lakes.

INTRODUCTION

Between 1993 and 2003, Greenland contributed $0.21 \pm 0.07 \text{ mm a}^{-1}$ to global mean sea-level rise (Lemke and others, 2007). This contribution is projected to increase to $0.3\text{--}1.9 \text{ mm a}^{-1}$ for the period 2090–99 (Meehl and others, 2007). While some of the present and projected contribution is from direct meltwater runoff, most of the contribution is due to changes in ice dynamics, namely faster flow velocities of outlet glaciers, and the resultant increase in the calving of solid ice into the oceans. Enhanced surface meltwater generation can play a role in these flow-speed accelerations via increased subglacial lubrication facilitated by larger amounts of water reaching the bed (Boon and Sharp, 2003; Parizek and Alley, 2004; Van der Veen, 2007; Das and others, 2008; Bartholomew and others, 2010). Observational evidence supports this process (Zwally and others, 2002; Van de Wal and others, 2008; Shepherd and others, 2009) although its effect on outlet glacier speeds is unclear (Joughin and others, 2008). Our understanding of this complex process is limited, in part, by our knowledge of the minimum quantity of meltwater needed, and the timing of its availability, to initiate and sustain increased glacier flow rates (Parizek and Alley, 2004).

We previously developed a method for determining the depth and, hence, the volume of surface melt ponds by applying a radiative transfer model to multispectral Advanced Spaceborne Thermal Emission and Reflection Radiometer (ASTER) imagery (Sneed and Hamilton, 2007). In principle, the algorithm can also be applied to other types of visible imagery, such as Landsat 7 Enhanced Thematic Mapper Plus (ETM+), and Moderate Resolution Imaging Spectroradiometer (MODIS) satellite sensor images. The bands of interest are: VNIR1 (520–600 nm) and VNIR3N (780–860 nm) for ASTER; band 2 (525–605 nm) and band 4 (750–900 nm) for Landsat 7; and band 4 (545–565 nm) and band 2 (841–876 nm) for MODIS. The method used for extracting water depth and bottom albedo is based on Bouguer–Lambert–Beer's law

$$I(z, \lambda) = I(0, \lambda)e^{-(K_\lambda)(z)}, \quad (1)$$

where $I(z, \lambda)$ is the water-leaving spectral intensity at some depth, $I(0, \lambda)$ is the spectral intensity at zero depth, K_λ is the

spectral attenuation and z is depth. Written in terms of reflectance and inverted to logarithmic form (Philpot, 1989),

$$z = \left[\ln(A_d - R_\infty) - \ln(R_w - R_\infty) \right] / (-g), \quad (2)$$

where g is given below, A_d is the bottom or substrate albedo (reflectance), R_∞ is the reflectance for optically deep water and R_w is the reflectance of some pixel of interest. As a practical matter, R_∞ is reflectance from optically deep water where the influence of bottom reflectance is nil; it can be derived from water that is deeper than ~ 40 m. With values for R_∞ , g and R_w in hand, A_d must be determined before the water depth, z , of the pixel of interest can be calculated. Details of the procedure for determining A_d are given by Sneed and Hamilton (2007, section 2.3). The quantity g is

$$g \approx K_d + aD_u \quad (3)$$

where K_d is the diffuse attenuation coefficient for downwelling light, a is the beam absorption coefficient and D_u an upwelling light distribution function or the reciprocal of the upwelling average cosine (Mobley, 1994).

The depth retrieval algorithm contains several simplifying assumptions:

Suspended or dissolved, organic or inorganic, particulate matter is minimal.

There is no wind, and therefore there are no waves, on a pond's surface.

There is no inelastic scattering (e.g. Raman scattering or fluorescence).

The substrate of a melt pond is homogeneous and parallel to the surface.

An additional unstated assumption of Sneed and Hamilton (2007) is that the image containing surface meltwater and melt ponds must also contain optically deep water suitable for deriving R_∞ . In practice, this means that suitable images must cover both the ice-sheet margin and adjacent regions of ice-free ocean, a potential limitation for ASTER images which are only $65 \text{ km} \times 65 \text{ km}$ and the $185 \text{ km} \times 185 \text{ km}$ Landsat 7 ETM+ images.

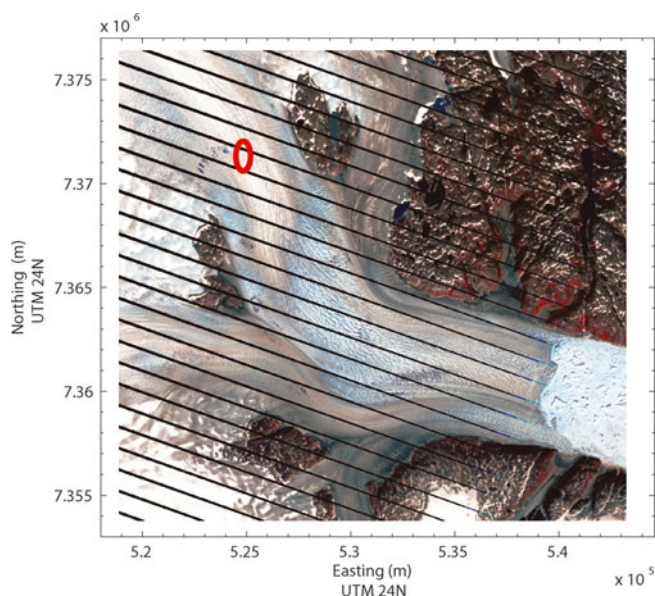


Fig. 1. A portion of the 20 July 2008 Landsat 7 image showing the melt ponds on Helheim Glacier, East Greenland. The red ellipse indicates the pond where the 11 July 2008 measurements were made.

Here we examine the validity of the above assumptions based on new theoretical analyses and field observations on an East Greenland melt pond in July 2008.

HELHEIM GLACIER, EAST GREENLAND

In situ data

On 11 July 2008 we carried out a depth survey of a melt pond on Helheim Glacier from a rowed, inflatable boat with simultaneous radiometric and global positioning (GPS) measurements. A digital fathometer with a measured accuracy of 0.03 m was used to collect water depths, and a Garmin[®] hand-held GPS provided position coordinates. A Satlantic Profiler II[®] (Satlantic, Inc., Halifax, Nova Scotia, Canada) with two hyperspectral radiometers (operated in the surface mode) was used to collect above- and below-water radiometric data. The downwelling surface irradiance radiometer with a cosine detector was positioned ~ 15 cm above the water surface while the upwelling, water-leaving radiance radiometer was positioned ~ 10 cm below the water surface. The radiometers were towed 5–10 m behind the boat and every effort was made to not cast a shadow on the pond bottom below the radiometers. Depth and GPS data were recorded by hand and radiometric data were collected on a laptop computer. The physical configuration of the Profiler II[®] precluded gathering radiometric data in water shallower than ~ 0.5 m, although depth and GPS measurements were made in shallow water.

Measurements began at 12:51 local time (UTC-2) and ended at 13:41 local time (UTC-2). There was no detectable wind, the pond surface was calm and the sky was clear except for a few scattered high clouds. Our somewhat meandering course covered a straight-line distance of ~ 200 m on the long axis of the pond and we recorded 21 depths and 3 GPS positions. The shallowest depth, of 0.7 m, was recorded near 66.46231° N, 038.45100° W (524465.0 E, 7371604.0 N UTM 24N) and the deepest depth,

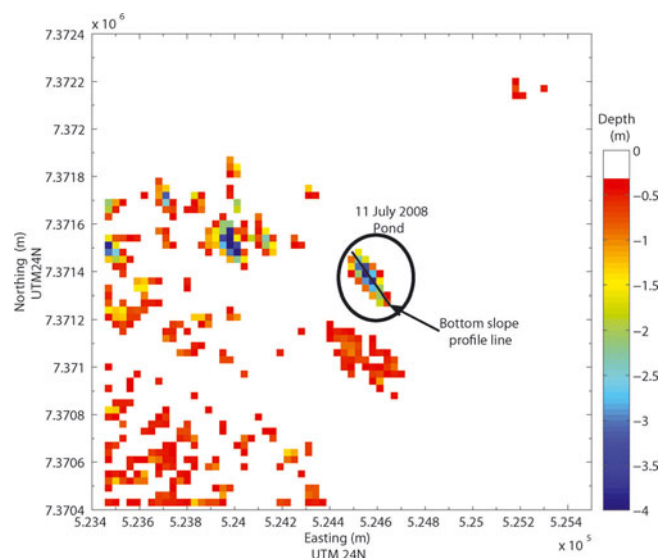


Fig. 2. A water-depth map of the melt pond where the 11 July measurements were made.

of 3.0 m, recorded near 66.46145° N, 038.44996° W (524512.0 E, 7371454.0 N UTM 24N). It should be noted that our deepest recorded depth was not necessarily the deepest part of the pond. We also observed a number of scattered cryoconite holes in the pond bottom that appeared to be ~ 5 – 15 cm in diameter. An examination of more than 3600 upwelling radiance, $L_w(0^-)$, values at 475 and 555 nm shows occasional sudden and transient decreases which probably indicate cryoconite holes.

Satellite-derived data

A satellite image from the Advanced Land Observing Satellite (ALOS, 10 m spatial resolution) for 22 June 2008 shows a roughly elliptical pond with a major axis of ~ 1200 m oriented in a northwest–southeast direction and a minor axis of ~ 500 m. An ASTER image of 3 August 2008 (15 m spatial resolution) shows the pond reduced to scattered segments; the area where the in situ data of 11 July were collected is completely devoid of water. However, a Landsat 7 (30 m spatial resolution) image of 20 July 2008 (path\row, 232\013) does contain the pond segment we measured on 11 July (Fig. 1) and was used to calculate water depths, using Equation (2). Another Landsat 7 image of 20 July (path\row, 232\014) provided the R_∞ data.

Both images were subsetting to speed up processing, converted to top-of-atmosphere reflectance (Irish, 1999), and atmospherically corrected using the 6SV radiative-transfer modeling code of Vermote and others (2005). Water depths were calculated following the procedures set out by Sneed and Hamilton (2007, section 2.3). The following numerical values were used to calculate the water depths shown in Figure 2: A_d , 0.5639; R_∞ , 0.0380; g , 0.1180 m^{-1} ; solar zenith, 47.0387° ; and an index of refraction for sea water of 1.33157. Because of the large spatial resolution of the Landsat image, it is not possible to attribute a measured depth at a particular location to a particular pixel in Figure 2. However, the depth map does show decreasing depths at the northwest and southeast ends of the pond and a deep area near the middle, all of which are consistent with the depths we measured at those locations.

ASSUMPTIONS

Suspended and dissolved matter

Meltwater samples were recovered from a melt pond on Helheim Glacier in July 2007 and July 2008 for detailed optical and chemical analyses. The melt pond lies ~100 km inland from the Atlantic Ocean at an elevation of ~600 m and is equidistant (~3 km) from two large nunataks. Not surprisingly, ion chromatography analysis of the water shows a strong marine influence. Methylsulfonate (MS^-) is present (2.12 and $0.40 \mu\text{g L}^{-1}$ in the 2007 and 2008 samples, respectively), and is an indirect product of marine biota (Legrand and Mayewski, 1997). The sodium (Na^+) and chloride (Cl^-) ratios for both years (0.545 and 0.515) are close to the sea-water (salinity, $S = 35$) ratio of 0.557 (Pilson, 1998) and are a further indication of a marine source. The concentrations of the other major ions (K^+ , Mg^{2+} , Ca^{2+} , NO_3^- and SO_4^{2-}) are consistent with the minimum concentrations found in snow throughout the Arctic. The calcium (Ca^{2+}), potassium (K^+) and magnesium (Mg^{2+}) are most likely derived from terrestrial dust, while the NO_3^- and SO_4^{2-} are linked to human activities (Legrand and Mayewski, 1997; De Caritat and others, 2005). The concentrations of K^+ and Mg^{2+} for both years are near the instrumental detection limit and are commensurate with the low levels of particulate scattering measured by the optical analyses below.

For the optical analyses, spectral transmittance and spectral absorption were measured at nine wavelengths using a WETLabs (Philomath, OR, USA) ac-9[®] absorption and attenuation meter. The spectral absorption coefficient, a , and the spectral beam attenuation coefficient, c , are derived from the ac-9 measurements. The ac-9 samples nine bands but we are primarily interested in the one centered at 555 nm, because it is very near the midpoints of the ASTER, Landsat and MODIS bands used to calculate water depth.

The absorption coefficient, a (particulate and dissolved) is near the instrument's resolution limits, $a = 0.003$ and 0.010 m^{-1} at 555 nm for 2007 and 2008, respectively. Particulate scattering, b , is not measured directly but derived from the energy equation, $c = a + b$. The scattering coefficients are $b = 0.050$ and 0.014 m^{-1} at 555 nm, in 2007 and 2008, respectively. By way of comparison, Smith and Baker (1981) analyzed fresh water from Crater Lake, Oregon, USA, and reported $a = 0.0638 \text{ m}^{-1}$ and $b = 0.0015 \text{ m}^{-1}$ at 550 nm while Davies-Colley (1983) reported on three shallow lakes in New Zealand with absorption coefficients, a , of ~ 0.5 – $\sim 1.4 \text{ m}^{-1}$ and scattering coefficients, b , of 3.2 – 30 m^{-1} at 550 nm.

The slopes of the spectral scattering curves for both years are very similar, as are the slopes of the concomitant particle-size distribution curves (Boss and others, 2001), indicating that the bulk of the particulate matter has a distribution similar to that of small particles (Babin and others, 2003). Babin and others (2003) showed the close relationship between an increasing backscattering coefficient, $b_b(\lambda)$, and an increase of suspended particulate matter measured by dry weight per unit volume of sea water (g m^{-3}). A similar relation should hold for backscatter coefficient and particle load in a freshwater melt pond, so any bias introduced by particulates in the calculated water depth will be minimal, given the small measured values of a and b in our samples.

Table 1. Shallow water wave amplitude as a function of wind speed, fetch and water depth

Wind speed	Fetch	Water depth	Wave amplitude	Wavelength
m s^{-1}	km	m	m	m
2	0.5	15	0.019	0.47
2	1.0	15	0.026	0.68
20	0.5	15	0.32	3.5
20	1.0	15	0.45	5.5
20	2.0	30	0.64	8.7

Wind and waves

Quantifying the effects of wind and the resultant waves on the water depth calculated using Equation (2) requires that we know the wind speed in the area of the melt pond. The large size (>1 km in diameter) of some ponds introduces the possibility that light could be specularly reflected from a wave facet to the satellite sensor, producing sun glint given the required confluence of solar and sensor relative azimuth, wind speed, wind direction and wave-facet slope. This is an unlikely scenario for most of the ice sheet, so instead we take a modeling approach. Consider a circular pond with a diameter of 1 km and an idealized uniform depth of 15 m. It is possible to calculate wave amplitudes for a given wind speed, water depth and fetch from first principles (e.g. http://woodshole.er.usgs.gov/staffpages/csherwood/sedx_equations/RunSPMWave.html; Table 1).

Zaneveld and others (2001) modeled remote-sensing reflectance, R_{rs} , as a function of wave amplitude and the angle between the light source and the sensor at a small fixed wavelength, 0.01 m. A conservative value for this angle using an ASTER image is 5° . Given the first four wave amplitudes in Table 1 and a look angle of 5° , R_{rs} would increase by $\sim 5\%$ with a 20 m s^{-1} wind, and, with the last set of values, R_{rs} might increase by 10–11% (Zaneveld and others, 2001, fig. 3). As the period and wavelength increase beyond the small value used by Zaneveld and others (2001) we expect the wave effect on remote-sensing reflectance (and other apparent optical properties) to diminish due to spatial averaging. To test the sensitivity of remote-sensing reflectance to surface wind speed, five modeling runs were performed using HYDROLIGHT[®]. We varied the wind speed between 0 and 14.9 m s^{-1} , the maximum allowed by the software, while holding all other input parameters fixed, and observed only a 1.4% decrease in the remote-sensing reflectance. Thus, we conclude that the effect of waves on the optical signal at the satellite, and derived water depths, is relatively unimportant.

Inelastic scattering

There is always inelastic scattering of light by natural waters (salt or fresh) at visible wavelengths. Molecular or Raman scattering is always present and fluorescence, due to dissolved or suspended organic material, can also occur. As particulate matter (organic or inorganic) decreases, the effects of elastic scattering on the in-water and above-water light fields diminishes and scattering is mainly by inelastic collisions. As fluorescence decreases, the contribution of Raman scattering to the light field becomes more

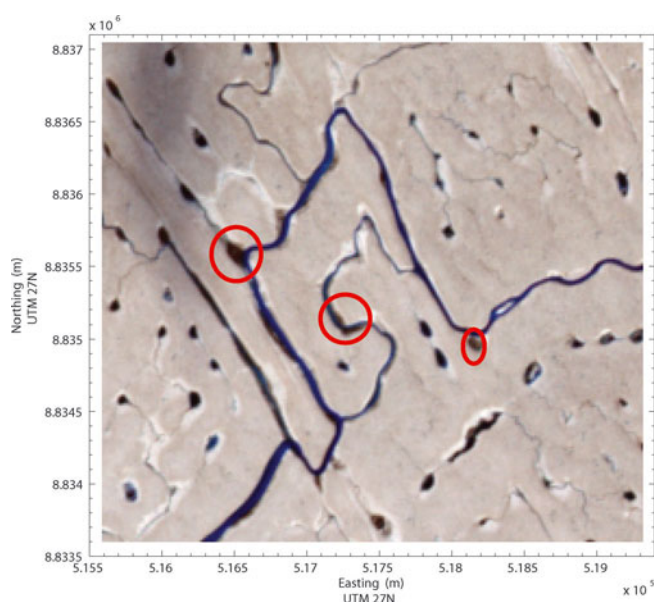


Fig. 3. A portion of an ASTER image (5 August 2009) of the Nioghalvfjordsfjorden glacier ice tongue, northeast Greenland, near the terminus. Red ellipses outline areas of cryoconite. This area was photographed from a helicopter by one of us (G.S.H.) in early September 2009, and a sample of cryoconite was retrieved.

pronounced (e.g. Morel and Gentili, 1991; Morel and Loisel, 1998). But, as Gordon (1999) points out, Raman scattering in natural waters is relevant to the remote sensing of ocean color and its use as a proxy for oceanic biological productivity. Here our interest is much simpler – to determine the depth of a glacial melt pond – and it is not necessary to partition the bulk scattering coefficient between elastic and inelastic collisions.

Substrate homogeneity and bottom slope

We originally assumed that the bottom of a melt pond or meltwater channel was ice with the same albedo throughout. However, we observed numerous cryoconite holes (~5–15 cm in diameter) in the bottom of the Helheim Glacier melt pond. These holes raise the possibility that larger areas of cryoconite might collect in the deepest parts of a pond or at the bends of a meltwater channel where water velocity slows. Detecting such areas and quantifying their effect on calculated water depth is not trivial, although the latter is the easier of the two problems.

Gadja (1958) described cryoconite as a fine, or very fine, dark, wind-blown dust composed of organic and/or inorganic material deposited on snow or ice surfaces, and Gerdell and Drouet (1960) described the color as dark brown to blue/black. Takeuchi (2002a) analyzed cryoconite from nine glaciers, three in the Himalaya, three in Tibet, one on

Baffin Island, one on Axel Heiberg and one on Spitsbergen, for organic and mineral content and spectral reflectance. Takeuchi and colleagues have also measured the spectral reflectance (albedo) of cryoconite in such diverse regions as Patagonia (Takeuchi and others, 2001), China (Takeuchi and Li, 2008) and Alaska (Takeuchi, 2002b; Takeuchi and others, 2003). Bøggild and others (2010) have measured the spectral albedo of surface cryoconite in northeast Greenland and their values agree well with those of Takeuchi. Thus, if we can detect cryoconite in satellite images, we can correct for its effects on the water-depth calculations. Areas of cryoconite are occasionally large enough to be detected in satellite images, as can be seen in Figure 3, an ASTER image with 15 m spatial resolution. In the case of Figure 3 it is a simple matter to mask out the cryoconite pixels before calculating the water depth and volume in this sub-image.

For pixels that might contain a mixture of cryoconite and water, spectral mixture analysis (SMA) can determine the fractions of each in a pixel (Adams and others, 1995; Tompkins and others, 1997). The method of Tompkins and others (1997) is especially useful because it requires no prior knowledge of the spectra of the components that might mix in a pixel. Nevertheless, the spectral analyses of Takeuchi and colleagues can provide good initial values for determining the end members. The use of SMA in conjunction with the depth algorithm of Sneed and Hamilton (2007) is the next step in the ongoing refinement of the algorithm.

We have also assumed the slope of the bottom for any given pixel is very small, i.e. that a bottom pixel is more or less parallel to the water surface. When there is a significant slope, the value of A_d , the bottom or substrate albedo (reflectance), can be overestimated by as much as 30% (Zaneveld and Boss, 2003). A ~400 m transect was struck across the melt ponds shown in Figure 2 which contained 12 data points, (Fig. 4). The points were evenly spaced along the transect, with the distance between any two points ~33 m, the approximate size of an ETM+ pixel. The bottom slope angles between adjacent data points were calculated. Figure 5 shows that for this transect the maximum slope angle between any two adjacent points is ~3.5°. Mobley and Sundman (2003) show that for slopes of 20° or less the upwelling radiance error is <10%. At angles of ~1° the percentage of error is almost zero (Mobley and Sundman, 2003, fig. 6). Our experience has shown that the bottom profile of most melt ponds closely resembles that of Figure 4, so any errors in A_d due to bottom slope angles will be very small.

Dark and deep water

Reflectance over optically deep water where the influence of bottom reflectance is nil, R_∞ , can be derived from water that is deeper than ~40 m and is one of the two end points needed to solve Equation (2), the other being A_d . Ideally, such water would be as similar to the melt pond water as

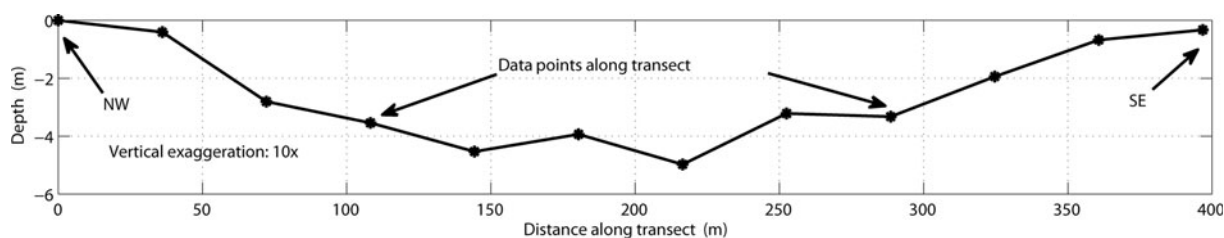


Fig. 4. Bottom profile of the 400 m transect.

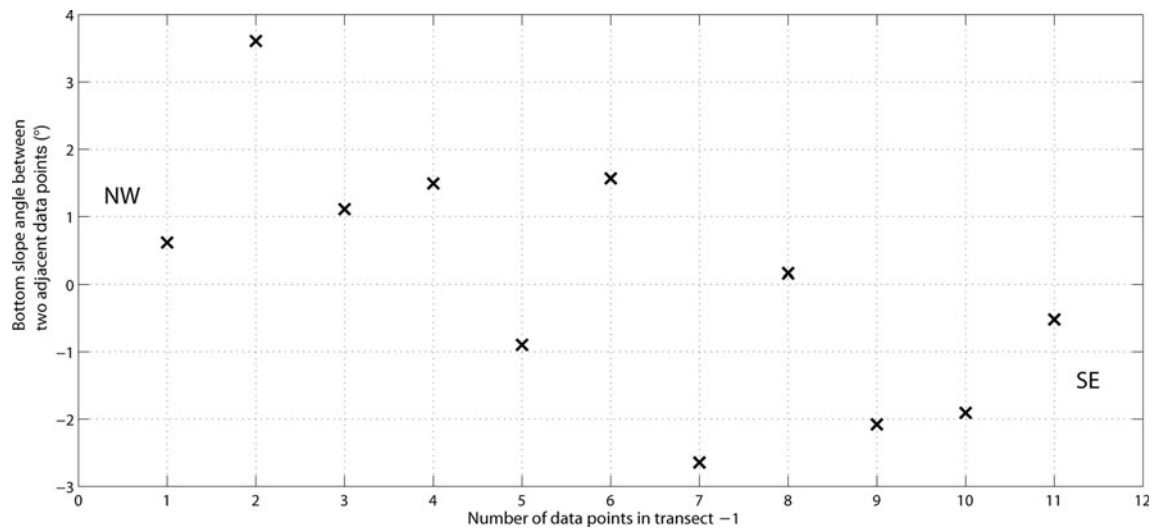


Fig. 5. Bottom slope angles. The angles are between adjacent data points of the 400 m melt pond transect.

possible, i.e. fresh water with low particle concentrations, and sufficiently deep that the bottom reflectance is nil. Absent such a water body, can we use deep ocean water as a source for R_{∞} and what adjustments (if any) must be made in Equation (3) to account for the differing water types?

Temperature, salinity and the beam absorption and scattering coefficients

Pegau and Zaneveld (1993, fig. 3) show that for six temperatures between 5 and 30°C, the absorption spectra of fresh and salt water from 550 to 740 nm are virtually identical and Sullivan and others (2006) report no significant temperature dependence between 440 and 550 nm.

For both fresh water and filtered sea water (salinity of ~25 psu) and temperatures varying from 6 to 30°C, Trøbjerg and Høyerslev (1996) report the absorption coefficient temperature dependence to be $-0.00091 \pm 0.00006 \text{ m}^{-1} \text{ K}^{-1}$ in the 400–550 nm range, while Pegau and others (1997) report a temperature dependence of $<0.001 \text{ m}^{-1}$ in the range 400–700 nm for pure and salt water and temperatures between 15 and 30°C. Pegau and others (1997) suggest that the linear relationship between temperature and the absorption coefficient holds down to the lower temperatures found in the polar seas. It is reasonable to conclude that any temperature differences between a melt pond and a water body that is the source of R_{∞} will have a negligible effect on the absorption coefficient in the visible spectrum.

As is the case with temperature, Pegau and others (1997) find a very small salinity dependence for the absorption coefficient in the visible spectrum ($<0.00015 \text{ m}^{-1} (\text{psu})^{-1}$) the exception being, as with temperature, in the near-infrared. Pope and Fry (1997) report absorption coefficients of 0.00635 and 0.0565 m^{-1} for 440 and 550 nm, respectively. At 555 nm, a difference of 30 psu might reduce the absorption coefficient by 0.0009 m^{-1} (Pegau and others, 1997, table 4). Using Pope and Fry's absorption data for pure water, Sullivan and others (2006) conclude that pure sea water with a salinity of 36 psu would increase the absorption coefficient by $\leq 0.002 \text{ m}^{-1}$ over the spectral range 400–680 nm. We conclude that salinity differences between a melt pond and ocean water will have a negligible effect on the absorption coefficient in the visible spectrum (Mobley, 1994, ch. 3).

Both temperature and salinity affect the beam scattering coefficient, b , in the visible part of the spectrum (Mobley, 1994; Zhang and others, 2009). The scattering coefficient of pure sea water is ~30% greater than that of pure water (e.g. at 550 nm b is 0.00145 and 0.00195 m^{-1} for pure water and pure sea water, respectively; Mobley, 1994, table 3.8). However, the effects of temperature on both pure water and pure sea water are an order of magnitude smaller than those of salinity (Mobley, 1994, table 3.9). In optical remote sensing, the spectral backscattering coefficient, $b_b(\lambda)$, of incident light is of primary interest (see Mobley, 1994, ch. 3 for its derivation).

Particulate matter

The absorption coefficient, a , and the backscattering coefficient, $b_b(\lambda)$, are significantly modified by the concentration and type of particulate matter, although, in the clearest natural waters, scattering by water molecules may contribute 50–80% of the backscattering in the blue region (~500 nm) (Stramski and others, 2004), but the dissolved salts in ocean water contribute little to backscattering (Zhang and others, 2009). Such ocean water can be found near Easter Island in the southeastern Pacific Ocean (Morel and others, 2007) but may not be suitable for our purposes. Where might we find such clear water in the Arctic region?

Smith (1973) found 'optically very clear' water ~180 km northwest of Ellesmere Island and Pak and others (1977) found water ~50 km north of Ellesmere where 'the mass concentrations are very small, and typical of extremely clear ocean water'. Both study sites were near the 1000 m depth contour. In 1998 above the Chukchi plateau (~77° N; ~173° W) Pegau (2002) recorded beam attenuation measurements to be 25% larger than Smith (1973) and attributed the difference to increased levels of colored dissolved organic material (CDOM) brought into the Arctic Ocean by the large river systems of Eurasia and Canada and concluded that the water was not the clearest natural water. The inherent optical properties of coastal waters are dominated by terrigenous particulates, CDOM and phytoplankton but in deep ocean waters phytoplankton (living or not) dominate. Therefore, it is reasonable to restrict the search for the source water of R_{∞} far from shore in deep

Table 2. Volume changes for different R_{∞} images, Austfonna, Nordaustlandet, Svalbard

Trial	13 July 2004 volume	Difference of volume relative to trial 1
	10^6 m^3	%
1	5.62	n/a
2	5.61	-0.2
3	5.62	0.0
4	5.65	+0.5
5	7.41	+31.9
6	6.19	+10.1
7	5.69	+1.2
8	5.91	+5.2
9	5.69	+1.2
10asc	5.77	+2.7
11low	5.93	+5.5

water, away from river systems, and, in the Arctic, far from the meltwater plumes of tidewater glaciers.

Ocean water

To investigate whether it is necessary that the image containing meltwater also contain deep-water pixels and to test the sensitivity of volume calculations to varying values of R_{∞} , ten widely scattered (in space and time) ASTER images with deep ocean water were used to extract small, VNIR1 sub-images ($\sim 30 \times 30$ pixels) of only deep water. Two images are from northwestern Greenland, four from northeastern Greenland, one from southeastern Greenland and three from eastern and southeastern Svalbard. One of the northeastern Greenland images is an ascending pass and the southeastern Greenland image has a low gain setting for VNIR1, rather than a normal gain setting. The ten sub-images were corrected to provide top-of-atmosphere reflectance. An atmospherically corrected ASTER scene (13 July 2004) of a melt pond on the Austfonna ice cap, located on Nordaustlandet, Svalbard, was used to calculate the meltwater volume. One of the ten R_{∞} sub-images was derived from this 13 July 2004 image, and its R_{∞} value was used to calculate the first meltwater volume. The volumes calculated using the other nine R_{∞} sub-images are relative to this first volume. The true depth and volume of this pond are unknown. Table 2 shows the results of the volume calculations. The median volume for trials 2–11 is $5.73 \times 10^6 \text{ m}^3$, and the median percentage difference is 2.0%. If we exclude outliers, trials 5 and 6, the medians become $5.69 \times 10^6 \text{ m}^3$ and 1.2%, respectively. A close examination of the images used in trials 5 and 6 using the thermal infrared bands revealed that high, thin clouds covered both images used for R_{∞} .

The deep-water sub-images for trials 2, 3, 7 and 9 (those trials with the smallest percentage difference relative to trial 1) are from northeastern Svalbard, southeastern Svalbard, northeastern Greenland and northeastern Greenland, respectively. The image dates for these four trials are 7 July 2004, 4 July 2005, 21 August 2000 and 21 July 2003, respectively.

It is difficult to account for the considerable variation in percentage difference between trials 3 and 8. They are widely separate in space and time: southeastern Svalbard and northeastern Greenland and 4 July 2005 and 10 August

2000, respectively. Trial 8's sub-image does have the largest off-nadir pointing angle (-8.575°) of all the trials. However, there are not enough images with varying pointing angles to attempt an analysis of its effect on the calculated volume.

A similar test using Landsat 7 ETM+ images has not been undertaken, nor has one using MODIS images. A variable viewing angle is not an issue with Landsat; however, gain settings can vary depending on surface type and sun elevation angle (Irish, 1999). Given the large number of MODIS data products, the key consideration is to use one that is not a composite of daily orbits, pointing angles and gain settings (e.g. MOD02). As with ASTER images, care should be exercised when choosing 'blackest' deep water pixels.

NUMERICAL MODELING

A simple modeling exercise was carried out that compared the deepest depth derived using Equation (2) with that calculated by HYDROLIGHT[®] (Sequoia Scientific, Inc., Bellevue, WA, USA), a radiative transfer numerical modeling software. In situ, laboratory and satellite data provided the input parameters to HYDROLIGHT[®]. Additional model inputs of total ozone, column perceptible water vapor and surface pressure data were taken from MODIS, the MOD07 Atmospheric Profile data product for 11 July 2008. The maximum depth calculated by Equation (2) was 4.2 m while the modeled maximum depth (using the Petzold average particle phase function; Mobley, 1994) was 4.1 m, a difference of $\sim 2.4\%$.

CONCLUSIONS

When using the method for determining water depth set out by Sneed and Hamilton (2007) and Equation (2), it is reasonable to assume that inelastic scattering plays no part in that calculation while wind-generated surface waves have a very small effect on the derived depth. Furthermore, we have demonstrated that it is not necessary that the satellite image showing surface meltwater must also contain dark, infinitely deep water. Based on 3 years of water analyses of meltwater from eastern Greenland we are confident that dissolved or suspended particulate matter plays a minor role in accurately determining meltwater depth and volume. Nevertheless, a larger sample set would be welcome and we will continue to collect and analyze meltwater from different regions of Greenland. The assumption of substrate homogeneity remains somewhat problematic and warrants further investigation. Spectral mixture analysis may provide a method for determining what percentage of a pond's substrate with a different albedo from that of ice would significantly affect the derived depth and volume.

Given the 30 m resolution of Landsat 7 ETM+, in situ measured water depths agree reasonably well with those derived from a Landsat image, with the greatest depths found near the center of the pond and the shallowest at the edges. The numerically modeled maximum depth agrees very closely with that from the Landsat image.

ACKNOWLEDGEMENTS

G.S.H. is supported by NASA's Cryospheric Sciences Program and W.A.S. is supported by a NASA Earth and Space Science Fellowship. The Dan and Betty Churchill Fund

help defray a portion of the fieldwork costs. We thank E. Boss for the loan of radiometers, access to HYDROLIGHT[®] and discussions, and C. Roesler, W. Slade and M. Estapa for the optical analyses of water samples. We also thank S.B. Sneed for chemical analysis of water samples and J. Saros for the loan of an inflatable research vessel. Finally, thanks to two anonymous reviewers whose comments significantly improved the paper.

REFERENCES

- Adams, J.B. and 6 others. 1995. Classification of multispectral images based on fractions of endmembers: application to land-cover change in the Brazilian Amazon. *Remote Sens. Environ.*, **52**(2), 137–154.
- Babin, M., A. Morel, V. Fournier-Sicre, F. Fell and D. Stramski. 2003. Light scattering properties of marine particles in coastal and open ocean waters as related to the particle mass concentration. *Limnol. Oceanogr.*, **48**(2), 843–859.
- Bartholomew, I., P. Nienow, D. Mair, A. Hubbard, M.A. King and A. Sole. 2010. Seasonal evolution of subglacial drainage and acceleration in a Greenland outlet glacier. *Nature Geosci.*, **3**(6), 408–411.
- Bøggild, C.E., R.E. Brandt, K.J. Brown and S.G. Warren. 2010. The ablation zone in northeast Greenland: ice types, albedos and impurities. *J. Glaciol.*, **56**(195), 101–113.
- Boon, S. and M. Sharp. 2003. The role of hydrologically-driven ice fracture in drainage system evolution on an Arctic glacier. *Geophys. Res. Lett.*, **30**(18), 1916. (10.1029/2003GL018034.)
- Boss, E., M.S. Twardowski and S. Herring. 2001. Shape of the particulate beam attenuation spectrum and its inversion to obtain the shape of the particulate size distribution. *Appl. Opt.*, **40**(27), 4885–4893.
- Das, S.B. and 6 others. 2008. Fracture propagation to the base of the Greenland Ice Sheet during supraglacial lake drainage. *Science*, **320**(5877), 778–781.
- Davies-Colley, R.J. 1983. Optical properties and reflectance spectra of 3 shallow lakes obtained from a spectrophotometric study. *NZ J. Marine Freshw. Res.*, **17**(4), 445–459.
- De Caritat, P. and 8 others. 2011. Chemical composition of arctic snow: concentration levels and regional distribution of major elements. *Sci. Total Environ.*, **336**(1–3), 183–199.
- Gadja, R.T. 1958. Cryoconite phenomena on the Greenland ice cap in the Thule area. *Can. Geogr.*, **3**(12), 35–44.
- Gerdel, R.W. and F. Drouet. 1960. The cryoconite of the Thule area, Greenland. *Trans. Am. Microsc. Soc.*, **79**, 256–272.
- Gordon, H.R. 1999. Contribution of Raman scattering to water-leaving radiance: a reexamination. *Appl. Opt.*, **38**(15), 3166–3174.
- Irish, R.R. 1999. *Landsat-7 science data user's handbook*. Greenbelt, MD, NASA Goddard Space Flight Center. Landsat Project Science Office.
- Joughin, I., S.B. Das, M.A. King, B.E. Smith, I.M. Howat and T. Moon. 2008. Seasonal speedup along the western flank of the Greenland Ice Sheet. *Science*, **320**(5877), 781–783.
- Legrand, M. and P. Mayewski. 1997. Glaciochemistry of polar ice cores: a review. *Rev. Geophys.*, **35**(3), 219–243.
- Lemke, P. and 9 others. 2007. Observations: changes in snow, ice, and frozen ground. In Solomon, S. and 7 others, eds. *Climate change 2007: the physical science basis. Contribution of Working Group I to the Fourth Assessment Report of the Intergovernmental Panel on Climate Change*. Cambridge, etc., Cambridge University Press, 337–383.
- Meehl, G.A. and 12 others. 2007. Global climate projections. In Solomon, S. and 7 others, eds. *Climate change 2007: the physical science basis. Contribution of Working Group I to the Fourth Assessment Report of the Intergovernmental Panel on Climate Change*. Cambridge, etc., Cambridge University Press, 747–845.
- Mobley, C.D. 1994. *Light and water: radiative transfer in natural waters*. San Diego, etc., Academic Press.
- Mobley, C.D. and L.K. Sundman. 2003. Effects of optically shallow bottoms on upwelling radiances: inhomogeneous and sloping bottoms. *Limnol. Oceanogr.*, **48**(1/2), 329–336.
- Morel, A. and 6 others. 2007. Optical properties of the 'clearest' natural waters. *Limnol. Oceanogr.*, **52**(1), 217–229.
- Pak, H., R.E. Peterson and J.R.V. Zaneveld. 1977. Light scattering and suspended particulate matter in the Arctic Ocean north of Ellesmere Island. *J. Oceanogr.*, **33**(3), 131–136.
- Parizek, B.R. and R.B. Alley. 2004. Implications of increased Greenland surface melt under global-warming scenarios: ice-sheet simulations. *Quat. Sci. Rev.*, **23**(9–10), 1013–1027.
- Pegau, W.S. 2002. Inherent optical properties of the central Arctic surface waters. *J. Geophys. Res.*, **107**(C10), 1–7.
- Pegau, W.S. and J.R.V. Zaneveld. 1993. Temperature-dependent absorption of water in the red and near-infrared portions of the spectrum. *Limnol. Oceanogr.*, **38**(1), 188–192.
- Pegau, W.S., D. Gray and J.R.V. Zaneveld. 1997. Absorption and attenuation of visible and near-infrared light in water: dependence on temperature and salinity. *Appl. Opt.*, **36**(24), 6035–6046.
- Philpot, W.D. 1989. Bathymetric mapping with passive multi-spectral imagery. *Appl. Opt.*, **28**(8), 1569–1578.
- Pilson, M.E.Q. 1998. *An introduction to the chemistry of the sea*. Upper Saddle River, NJ, Prentice Hall.
- Pope, R.M. and E.S. Fry. 1997. Absorption spectrum (380–700 nm) of pure water. II. Integrating cavity measurements. *Appl. Opt.*, **36**(33), 8710–8723.
- Shepherd, A., A. Hubbard, P. Nienow, M. McMillan and I. Joughin. 2009. Greenland ice sheet motion coupled with daily melting in late summer. *Geophys. Res. Lett.*, **36**(1), L01501. (10.1029/2008GL035758.)
- Smith, R.C. 1973. Optical properties of the Arctic upper water. *Arctic*, **26**(4), 303–313.
- Smith, R.C. and K.S. Baker. 1981. Optical properties of the clearest natural waters (200–800 nm). *Appl. Opt.*, **20**(2), 177–184.
- Sneed, W.A. and G.S. Hamilton. 2007. Evolution of melt pond volume on the surface of the Greenland Ice Sheet. *Geophys. Res. Lett.*, **34**(3), L03501. (10.1029/2006GL028697.)
- Stramski, D., E. Boss, D. Bogucki and K.J. Voss. 2004. The role of seawater constituents in light backscattering in the ocean. *Progr. Oceanogr.*, **61**(1), 27–56.
- Sullivan, J.M. and 6 others. 2006. Hyperspectral temperature and salt dependencies of absorption by water and heavy water in the 400–750 nm spectral range. *Appl. Opt.*, **45**(21), 5294–5309.
- Takeuchi, N. 2002a. Optical characteristics of cryoconite (surface dust) on glaciers: the relationship between light absorbency and the property of organic matter contained in the cryoconite. *Ann. Glaciol.*, **34**, 409–414.
- Takeuchi, N. 2002b. Surface albedo and characteristics of cryoconite (biogenic surface dust) on an Alaska glacier, Gulkana Glacier in the Alaska Range. *Bull. Glaciol. Res.*, **19**, 63–70.
- Takeuchi, N. and Z. Li. 2008. Characteristics of surface dust on Ürümqi Glacier No. 1 in the Tien Shan Mountains, China. *Arct. Antarct. Alp. Res.*, **40**(4), 744–750.
- Takeuchi, N., S. Kohshima, T. Shiraiwa and K. Kubota. 2001. Characteristics of cryoconite (surface dust on glaciers) and surface albedo of a Patagonian glacier, Tyndall Glacier, Southern Patagonia Icefield. *Bull. Glaciol. Res.*, **18**, 65–69.
- Takeuchi, N., S. Kohshima and T. Segawa. 2003. Effect of cryoconite and snow algal communities on surface albedo on maritime glaciers in south Alaska. *Bull. Glaciol. Res.*, **20**, 21–27.
- Tompkins, S., J.F. Mustard, C.M. Pieters and D.W. Forsyth. 1997. Optimization of endmembers for spectral mixture analysis. *Remote Sens. Environ.*, **59**(3), 472–489.
- Trabjerg, I. and N.K. Høyerslev. 1996. Temperature influence on light absorption by fresh water and seawater in the visible and near-infrared spectrum. *Appl. Opt.*, **35**(15), 2653–2658.

- Van de Wal, R.S.W. and 6 others. 2008. Large and rapid melt-induced velocity changes in the ablation zone of the Greenland Ice Sheet. *Science*, **321**(5885), 111–113.
- Van der Veen, C.J. 2007. Fracture propagation as means of rapidly transferring surface meltwater to the base of glaciers. *Geophys. Res. Lett.*, **34**(1), L01501. (10.1029/2006GL028385.)
- Vermote, E., D. Tanré, J.L. Deuzé, M. Herman, J.J. Morcrette and S.Y. Kotchenova. 2005. *Second simulation of a satellite signal in the solar spectrum – vector (6SV)*. Greenbelt, MD, NASA Goddard Space Flight Center.
- Zaneveld, J.R.V. and E. Boss. 2003. The influence of bottom morphology on reflectance: theory and two-dimensional geometry model. *Limnol. Oceanogr.*, **48**(1/2), 374–379.
- Zaneveld, J.R.V., E. Boss and P. Hwang. 2001. The influence of coherent waves on the remotely sensed reflectance. *Optics Express*, **9**(6), 260–266.
- Zhang, X., L. Hu and M.X. He. 2009. Scattering by pure seawater: effect of salinity. *Optics Express*, **17**(7), 5698–5710.
- Zwally, H.J., W. Abdalati, T. Herring, K. Larson, J. Saba and K. Steffen. 2002. Surface melt-induced acceleration of Greenland ice-sheet flow. *Science*, **297**(5579), 218–222.